



# ALMA CO observations of a giant molecular cloud in M 33: Evidence for high-mass star formation triggered by cloud–cloud collisions

Hidetoshi SANO  <sup>1,\*</sup>, Kisetsu TSUGE  <sup>2</sup>, Kazuki TOKUDA  <sup>3,1</sup>, Kazuyuki MURAOKA  <sup>3</sup>, Kengo TACHIHARA  <sup>2</sup>, Yumiko YAMANE  <sup>2</sup>, Mikito KOHNO  <sup>4,2</sup>, Shinji FUJITA  <sup>2</sup>, Rei ENOKIYA  <sup>2</sup>, Gavin ROWELL  <sup>5</sup>, Nigel MAXTED  <sup>6</sup>, Miroslav D. FILIPOVIĆ  <sup>7</sup>, Jonathan KNIES, <sup>8</sup> Manami SASAKI  <sup>8</sup>, Toshikazu ONISHI  <sup>4</sup>, Paul P. PLUCINSKY  <sup>9</sup>, and Yasuo FUKUI  <sup>2,10</sup>

<sup>1</sup>National Astronomical Observatory of Japan, 2-21-1 Osawa, Mitaka, Tokyo 181-8588, Japan

<sup>2</sup>Department of Physics, Nagoya University, Furo-cho, Chikusa-ku, Nagoya, Aichi 464-8601, Japan

<sup>3</sup>Department of Physical Science, Graduate School of Science, Osaka Prefecture University, 1-1 Gakuen-cho, Naka-ku, Sakai, Osaka 599-8531, Japan

<sup>4</sup>Astronomy Section, Nagoya City Science Museum, 2-17-1 Sakae, Naka-ku, Nagoya, Aichi 460-0008, Japan

<sup>5</sup>School of Physical Sciences, The University of Adelaide, North Terrace, Adelaide, SA 5005, Australia

<sup>6</sup>School of Science, University of New South Wales, Australian Defence Force Academy, Canberra, ACT 2600, Australia

<sup>7</sup>Western Sydney University, Locked Bag 1797, Penrith South DC, NSW 2751, Australia

<sup>8</sup>Dr. Karl Remeis-Sternwarte, Erlangen Centre for Astroparticle Physics, Friedrich-Alexander-Universität Erlangen-Nürnberg, Sternwartstraße 7, D-96049 Bamberg, Germany

<sup>9</sup>Harvard-Smithsonian Center for Astrophysics, 60 Garden St., Cambridge, MA 02138, USA

<sup>10</sup>Institute for Advanced Research, Nagoya University, Furo-cho, Chikusa-ku, Nagoya, Aichi 464-8601, Japan

\*E-mail: hidetoshi.sano@nao.ac.jp

Received 2019 August 19; Accepted 2020 April 16

## Abstract

We report the first evidence for high-mass star formation triggered by collisions of molecular clouds in M 33. Using the Atacama Large Millimeter/submillimeter Array, we spatially resolved filamentary structures of giant molecular cloud 37 in M 33 using  $^{12}\text{CO}(J = 2-1)$ ,  $^{13}\text{CO}(J = 2-1)$ , and  $\text{C}^{18}\text{O}(J = 2-1)$  line emission at a spatial resolution of  $\sim 2\text{ pc}$ . There are two individual molecular clouds with a systematic velocity difference of  $\sim 6\text{ km s}^{-1}$ . Three continuum sources representing up to  $\sim 10$  high-mass stars with spectral types of B0V–O7.5V are embedded within the densest parts of molecular clouds bright in the  $\text{C}^{18}\text{O}(J = 2-1)$  line emission. The two molecular clouds show a complementary spatial distribution with a spatial displacement of  $\sim 6.2\text{ pc}$ , and show a V-shaped structure in the position–velocity diagram. These observational features traced by CO and its isotopes

are consistent with those in high-mass star-forming regions created by cloud–cloud collisions in the Galactic and Magellanic Cloud H $\text{II}$  regions. Our new finding in M 33 indicates that cloud–cloud collision is a promising process for triggering high-mass star formation in the Local Group.

**Key words:** ISM: H $\text{II}$  regions — ISM: individual objects (M 33, M 33GMC 37) — stars: formation

## 1 Introduction

It is a long-standing question how high-mass stars are formed in galaxies. Three different hypotheses are monolithic collapse, competitive accretion, and stellar mergers (e.g., Zinnecker & Yorke 2007 and references therein). However, these theoretical models have remained controversial due to the lack of conclusive observational evidence.

Recently, the alternative idea of high-mass star formation triggered by “cloud–cloud collisions” has received much attention since the discovery of 50 or more pieces of observational evidence (e.g., Fukui et al. 2018a; Enokiya et al. 2019 and references therein). The colliding clouds have a supersonic velocity difference with an intermediate velocity component—bridging feature—created by the collisional deceleration. The complementary spatial distribution of two clouds (or spatial anti-correlation between the two clouds) is an important signature of collisions because one of the colliding clouds can create a hollowed-out structure in the other cloud. Furthermore, a V-shaped structure can be seen in the position–velocity diagram due to the deceleration and hollowed-out structure. Theoretical studies also support these observational signatures, and predict that cloud–cloud collision increases the effective Jeans mass so high-mass stars can form in the shock-compressed layer (e.g., Habe & Ohta 1992; Anathpindika 2010; Inoue & Fukui 2013; Takahira et al. 2014; Shima et al. 2018; Inoue et al. 2018).

Investigating the universality of the cloud–cloud collision scenario, we need further observational examples in various environments and scales. In the individual Galactic star-forming regions such as Orion and Vela, high-mass star formation can be understood by at least five cloud–cloud collisions on  $\sim$ 1–100 pc scales (Fukui et al. 2016, 2018a; Fujita et al. 2020a; Sano et al. 2018; Hayashi et al. 2018; Enokiya et al. 2018). It is remarkable that collisions of molecular clouds are seen not only in our Milky Way, but also in the Magellanic Clouds (e.g., Fukui et al. 2015; Saigo et al. 2017). Furthermore, tidally driven galactic-scale (a few kpc scale) collisions of H $\text{I}$  clouds are found in the Magellanic and M31–M 33 systems (Fukui et al. 2017, 2019; Tachihara et al. 2018; Tsuge et al. 2019; Tokuda et al. 2019). We can therefore reveal sites of cloud–cloud

collisions even in external galaxies if the spatial resolution of CO/H $\text{I}$  data is high enough (e.g., a few pc scale).

Here, we report the first evidence for high-mass star formation triggered by collisions of molecular clouds in M 33. Sections 2 and 3 describe the observations and data reduction of the ALMA CO and continuum datasets and their results. Subsection 4.1 gives the properties of high-mass stars in the region; subsection 4.2 discuss the stellar feedback effect, and subsection 4.3 presents a possible scenario of cloud–cloud collision as the formation mechanism of high-mass stars. A summary and conclusions are provided in section 5.

## 2 Observations and data reduction

We carried out ALMA Band 6 (211–275 GHz) observations toward M 33GMC 37 in Cycle 6 as part of the CO survey toward the supernova remnants in M 33 (PI: H. Sano, #2018.1.00378.S). We used the single-pointing observation mode with 45–49 antennas of the 12 m arrays. The center position of the pointing is ( $\alpha_{\text{J}2000.0}, \delta_{\text{J}2000.0}$ )  $\sim$  (01 $^{\text{h}}33^{\text{m}}35^{\text{s}}.9, 30^{\circ}36'27''.5$ ). The baseline length ranges from 15.06 to 1397.85 m, corresponding to  $u - v$  distances from 11.6 to 1074.9  $k\lambda$ . The maximum recoverable scale (a.k.a. largest angular scale) is calculated to be 3. $''$ 73. Two quasars, J2253+1608 and J0237+2848, were observed as bandpass and flux calibrators. We also observed the quasar J0112+3208 as a phase calibrator. There were two spectral windows including the  $^{12}\text{CO}(J = 2-1)$ ,  $^{13}\text{CO}(J = 2-1)$ , and  $\text{C}^{18}\text{O}(J = 2-1)$  line emission with a bandwidth of 117.19 MHz. The frequency resolution was 70.6 kHz for  $^{12}\text{CO}(J = 2-1)$ , and 141.1 kHz for  $^{13}\text{CO}(J = 2-1)$  and  $\text{C}^{18}\text{O}(J = 2-1)$ . We also observed two spectral windows as continuum bands, with frequency ranges 231.0–233.0 GHz and 216.3–218.2 GHz. Although these continuum bands contain line emissions of H(30 $\alpha$ ) and SiO( $J = 5-4$ ), we could not detect the two lines significantly.

The data reduction was performed using the Common Astronomy Software Application (CASA; McMullin et al. 2007) package version 5.5.0. We used the “multiscale CLEAN” algorithm implemented in CASA (Cornwell 2008). The synthesized beam of the final dataset is

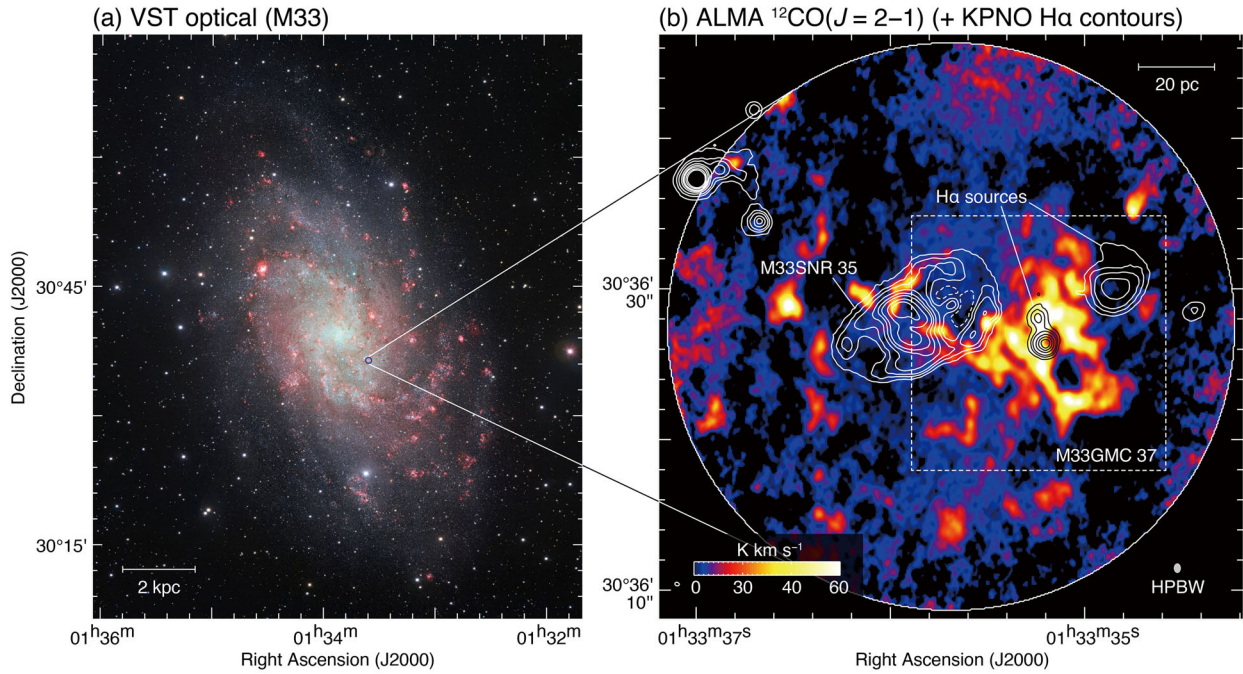


**Fig. 1.** (a) False color image of M 33 obtained with the VLT Survey Telescope (VST, credit: ESO). The red, orange, and cyan represent H $\alpha$ , r band, and g band, respectively. The blue circle indicates the ALMA FoV. The scale bar is shown in the bottom left corner. (b) Integrated intensity map of  $^{12}\text{CO}(J = 2-1)$  obtained with ALMA. The integration velocity range is  $-145$  to  $-126 \text{ km s}^{-1}$ . The superposed white and black contours indicate the H $\alpha$  intensity obtained by the Kitt Peak National Observatory (KPNO; Massey et al. 2006). The contour levels are 300, 400, 500, 700, 900, 1100, 1500, and  $1900 \text{ erg s}^{-2} \text{ cm}^{-2}$ . The dashed box containing M 33GMC 37 represents the region to be shown in figures 2, 4, 7, and 8. We also show the positions of M 33SNR 35 and H $\alpha$  sources. The scale bar and beam size are also shown in the top right and bottom right corners, respectively. (Color online)

$0.^{\circ}59 \times 0.^{\circ}42$  with a position angle (P.A.) of  $0.^{\circ}4$  for  $^{12}\text{CO}(J = 2-1)$ ,  $0.^{\circ}62 \times 0.^{\circ}44$  with a P.A. of  $0.^{\circ}1$  for  $^{13}\text{CO}(J = 2-1)$ ,  $0.^{\circ}63 \times 0.^{\circ}44$  with a P.A. of  $1.^{\circ}1$  for  $\text{C}^{18}\text{O}(J = 2-1)$ , and  $0.^{\circ}59 \times 0.^{\circ}43$  with a P.A. of  $-1.^{\circ}4$  for the 1.3 mm continuum. The typical spatial resolution is  $\sim 2 \text{ pc}$  at the distance of M 33 ( $817 \pm 59 \text{ kpc}$ ; Freedman et al. 2001). The typical noise fluctuations of the line emission and continuum are  $\sim 0.15 \text{ K}$  at the velocity resolution of  $1 \text{ km s}^{-1}$  and  $0.017 \text{ mJy beam}^{-1}$ , respectively. To estimate the missing flux density, we used the  $^{12}\text{CO}(J = 2-1)$  dataset obtained with the IRAM 30 m radio telescope (Gratier et al. 2010; Druard et al. 2014). Following the methods of Druard et al. (2014), we applied a forward efficiency of 0.92 and a main beam efficiency of 0.56 to convert the main beam temperature scale. We compared the integrated intensities of IRAM and ALMA CO data smoothed to match the FWHM resolution of  $12''$ . As a result, we found no significant difference within the error margins, and hence the missing flux density is considered to be negligible.

### 3 Results

Figure 1a shows an optical composite image of M 33 obtained with the VLT Survey Telescope (VST). The ALMA field of view (FoV) includes several H $\text{II}$  regions located in a spiral arm near the galactic center. Figure 1b shows a

large-scale map of ALMA  $^{12}\text{CO}(J = 2-1)$  superposed on H $\alpha$  contours. A giant molecular cloud (GMC)—M 33GMC 37—is mainly located on the western half of the ALMA FoV with filamentary structures. Some of the CO filaments are likely associated with M 33SNR 35, which will be described in a forthcoming paper (H. Sano et al. in preparation). We also note that a bright H $\alpha$  source with two local peaks at the positions ( $\alpha_{\text{J2000.0}}, \delta_{\text{J2000.0}}$ )  $\sim (01^{\text{h}}33^{\text{m}}35^{\text{s}}.24, 30^{\circ}36'28.''0)$  and  $(01^{\text{h}}33^{\text{m}}35^{\text{s}}.20, 30^{\circ}36'26.''3)$  are superposed on the GMC.

To derive the mass of a GMC, we used the following equations:

$$M = m_{\text{H}} \mu D^2 \Omega \sum_i [N_i(\text{H}_2)], \quad (1)$$

$$N(\text{H}_2) = X_{\text{CO}} \cdot W(\text{CO}_{10}), \quad (2)$$

where  $m_{\text{H}}$  is the mass of hydrogen,  $\mu$  is the mean molecular weight of  $\sim 2.74$ ,  $D$  is the distance to M 33 in units of cm,  $\Omega$  is the solid angle of each data pixel,  $N_i(\text{H}_2)$  is the column density of molecular hydrogen for each data pixel  $i$  in units of  $\text{cm}^{-2}$ ,  $X$  is the CO-to-H $_2$  conversion factor in units of  $(\text{K km s}^{-1})^{-1} \text{ cm}^{-2}$ , and  $W(\text{CO}_{10})$  is the integrated intensity of  $^{12}\text{CO}(J = 1-0)$  line emission. In the present study, we adopt  $D = 2.5 \times 10^{24} \text{ cm}$ , corresponding to the

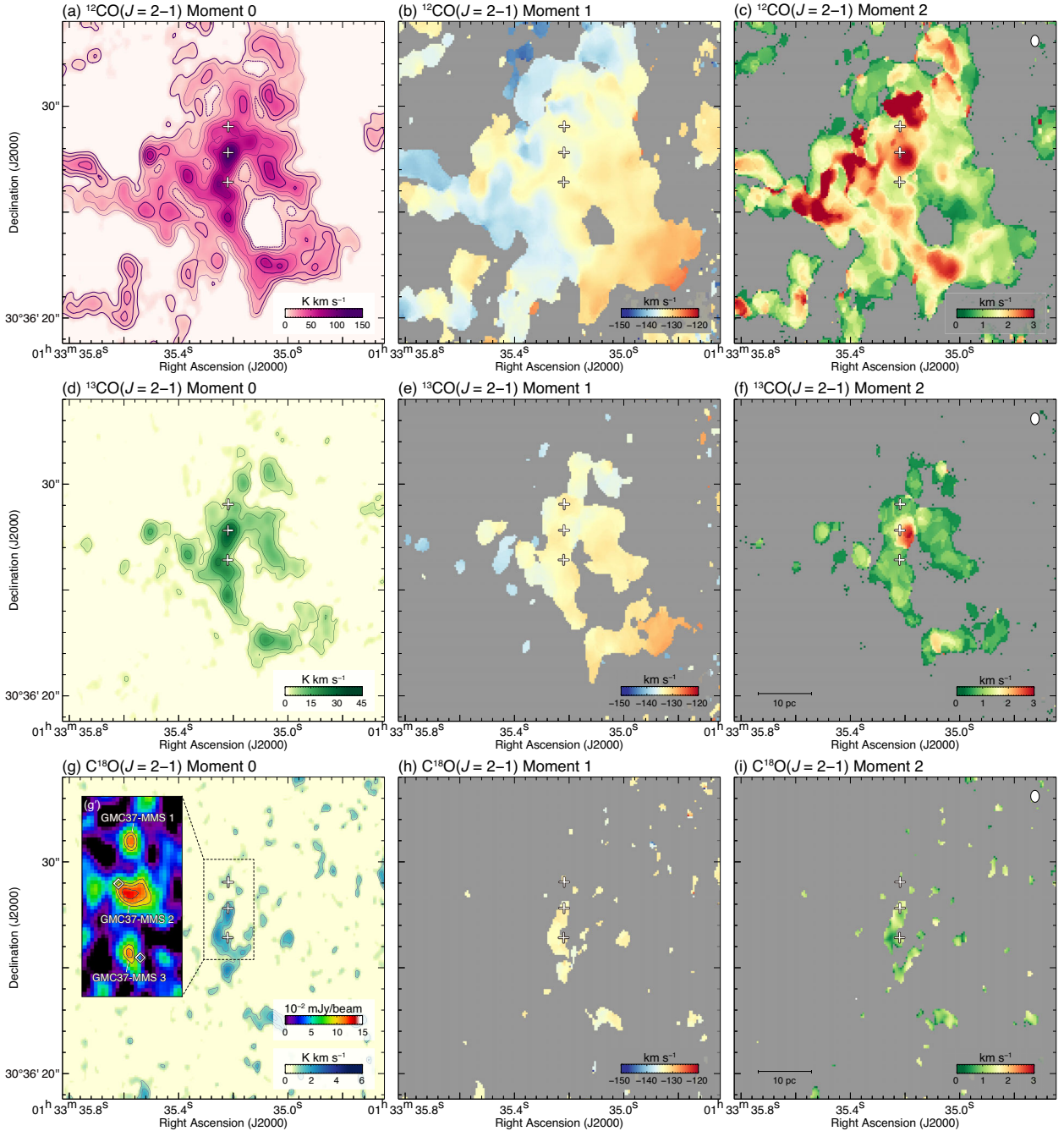


**Fig. 2.** Maps of moment 0 [integrated intensity: (a), (d), and (g)], moment 1 [peak velocity: (b), (e), and (h)], and moment 2 [velocity dispersion: (c), (f), and (i)] toward M33GMC 35 for each line emission. The contour levels of the moment 0 maps are 8, 14, 22, 32, 44, 58, 74, and 92  $\text{K km s}^{-1}$  for  $^{12}\text{CO}(J = 2-1)$ ; 4, 8, 14, and 22  $\text{K km s}^{-1}$  for  $^{13}\text{CO}(J = 2-1)$ ; and 1, 1.5, 2, 3, and 5  $\text{K km s}^{-1}$  for  $\text{C}^{18}\text{O}(J = 2-1)$ . The intensity distribution of the 1.3 mm continuum is also shown in panel (g'). The contour levels of the millimeter continuum are 9.0, 10.5, and  $12.0 \times 10^{-2} \text{ mJy beam}^{-1}$ . The crosses and diamonds represent the intensity peak positions of millimeter continuum sources and H $\alpha$ . The beam size and scale bar are also shown in the top right and bottom left corners of panels (c), (f), and (i), respectively. (Color online)

distance of 817 kpc (Freedman et al. 2001). Following the previous study by Gratier et al. (2012), we used  $X = 4.0 \times 10^{20} (\text{K km s}^{-1})^{-1} \text{ cm}^{-2}$ . We also derived a typical intensity ratio of  $^{12}\text{CO}(J = 2-1)/^{12}\text{CO}(J = 1-0)$  of  $\sim 0.7$  toward M33GMC 37 through comparison with an archival  $^{12}\text{CO}$  ( $J = 1-0$ ) data cube obtained with the Nobeyama Radio

Observatory 45 m telescope (Tosaki et al. 2011). Finally, the derived size and mass of the GMC are  $\sim 60$  pc and  $\sim 5 \times 10^5 M_\odot$ , respectively. These values are roughly consistent with the previous study by Miura et al. (2012) using the Atacama Submillimeter Telescope Experiment [a size of  $63 \times 54$  pc and virial mass of  $(6.7 \pm 4.8) \times 10^5 M_\odot$ ].

**Table 1.** Physical properties of 1.3 mm continuum sources.\*

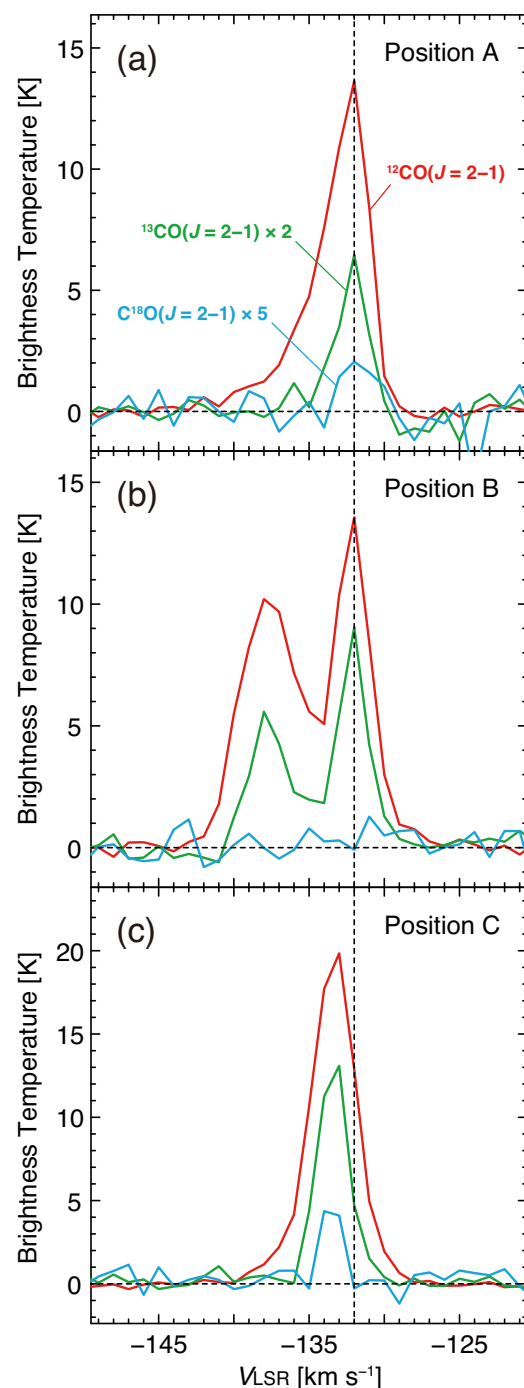
Name	$\alpha_{J2000.0}$ (h m s)	$\delta_{J2000.0}$ (° ' '')	$F_{\text{peak}}$ (mJy beam $^{-1}$ )	Size (pc)
(1)	(2)	(3)	(4)	(5)
GMC 37-MMS 1	01 33 35.22	30 36 29.0	0.12	1.7
GMC 37-MMS 2	01 33 35.22	30 36 27.8	0.13	3.0
GMC 37-MMS 3	01 33 35.22	30 36 26.4	0.11	1.6

\*Column (1): Name of millimeter continuum source. Columns (2)–(3): Positions of the maximum flux. Column (4): Peak flux of 1.3 mm continuum. Column (5): Size of continuum source defined as  $(S/\pi)^{0.5} \times 2$ , where  $S$  is the total surface area of the continuum source surrounded by a contour of the  $5\sigma$  level.

Figures 2a, 2d, and 2g show the maps of moment 0 (integrated intensity) for each line emission toward M 33GMC 37. The area shown in figure 2 is indicated by the dashed box in figure 1. The  $^{12}\text{CO}(J = 2-1)$  clouds are detected as diffuse emission with a ring-like structure in the southwest, while the  $^{13}\text{CO}(J = 2-1)$  clouds are only bright in the ring-like structure. The  $\text{C}^{18}\text{O}(J = 2-1)$  clouds are concentrated in the central region of the GMC where the  $^{12}\text{CO}(J = 2-1)$  and  $^{13}\text{CO}(J = 2-1)$  clouds are bright. We also find that there are three sources in the 1.3 mm continuum, as shown in figure 2g' (GMC 37-MMSs 1–3, hereafter referred to as MMSs 1–3), which are detected at a  $5\sigma$  level or higher. The basic physical properties of the three continuum sources are listed in table 1. The peak brightness temperatures of the three sources are comparable, but the spatial extent of MMS 2 is twice as large as for MMSs 1 and 3. It is possible that these millimeter continuum sources are physically related to the  $\text{H}\alpha$  emission. In particular, two of them (MMSs 2 and 3) are located in the vicinity of the two  $\text{H}\alpha$  peaks (as shown by diamonds in figure 2g') associated with the brightest CO cloud, indicating that the exciting stars of MMSs 2–3 and  $\text{H}\alpha$  peaks are the same. These regions are also bright in the Spitzer 24  $\mu\text{m}$  image (Verley et al. 2007).

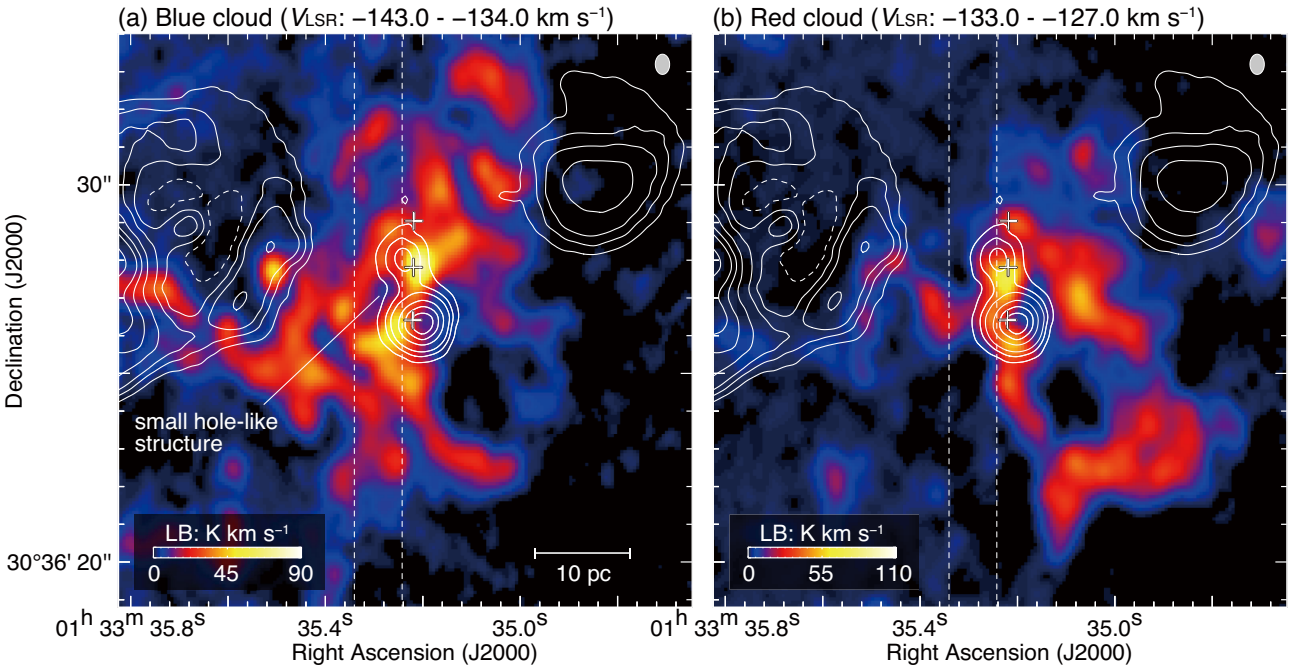
Figures 2b, 2e, and 2h show the maps of moment 1 (peak velocity). The peak velocities of the  $^{12}\text{CO}(J = 2-1)$  and  $^{13}\text{CO}(J = 2-1)$  clouds are discontinuous, with a velocity jump of  $\sim 10 \text{ km s}^{-1}$  toward the millimeter continuum sources and their eastern side, while that of the  $\text{C}^{18}\text{O}(J = 2-1)$  line emission shows no significant velocity jump within the clouds. Figures 2c, 2f, and 2i show the maps of moment 2 (velocity dispersion). A larger velocity dispersion above  $3 \text{ km s}^{-1}$  is seen in several regions of both the  $^{12}\text{CO}(J = 2-1)$  and  $^{13}\text{CO}(J = 2-1)$  clouds, where the velocity jumps are identified (see also figure 2b). On the other hand, there is no sign of such larger velocity dispersion in the  $\text{C}^{18}\text{O}(J = 2-1)$  clouds.

Figure 3 shows the typical CO spectra toward three positions, A, B, and C. Position A represents the direction of



**Fig. 3.** Typical CO spectra for the positions A [ $(\alpha_{J2000.0}, \delta_{J2000.0}) = (01^{\text{h}}33^{\text{m}}35^{\text{s}}22, 30^{\circ}36'29.''0)$ ], B [ $(\alpha_{J2000.0}, \delta_{J2000.0}) = (01^{\text{h}}33^{\text{m}}35^{\text{s}}19, 30^{\circ}36'27.''6)$ ], and C [ $(\alpha_{J2000.0}, \delta_{J2000.0}) = (01^{\text{h}}33^{\text{m}}35^{\text{s}}25, 30^{\circ}36'26.''6)$ ]. The  $^{13}\text{CO}(J = 2-1)$  and  $\text{C}^{18}\text{O}(J = 2-1)$  brightness temperatures are multiplied by a factor of two and five, respectively. The vertical dashed line indicates the systemic velocity of M 33GMC 37. (Color online)

MMS 1. Positions B and C correspond to the regions with the largest velocity dispersion in the  $^{13}\text{CO}(J = 2-1)$  line emission (see also figure 2f) and the maximum intensity of the  $\text{C}^{18}\text{O}(J = 2-1)$  line emission (see also figure 2g), respectively. The CO spectra of position A is centered at



**Fig. 4.** Integrated intensity maps of  $^{12}\text{CO}(J = 2-1)$ . The velocity range is  $-143$  to  $-134 \text{ km s}^{-1}$  for panel (a) and  $-133$  to  $-127 \text{ km s}^{-1}$  for panel (b). The vertical dashed lines indicate the integration range in RA for figure 5. The crosses represent the positions of the  $1.3 \text{ mm}$  continuum. The white contours indicate  $\text{H}\alpha$  emission as shown in figure 1b. The scale bar and beam size are also shown in the bottom and top right corners for each panel. (Color online)

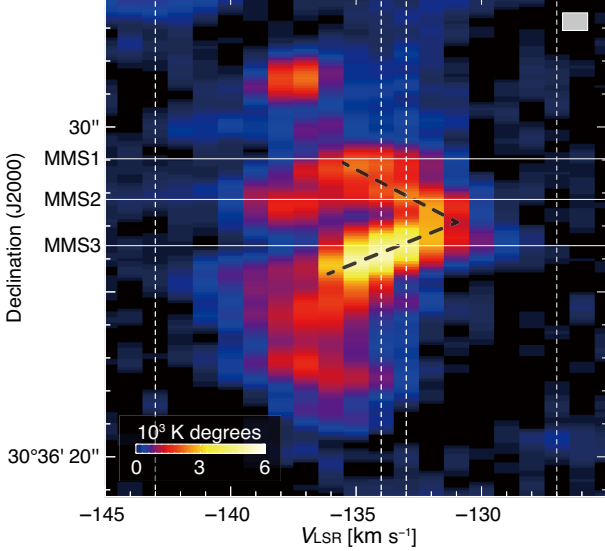


**Fig. 5.** Declination-velocity diagram of  $^{12}\text{CO}(J = 2-1)$ . The integration range is from  $01^{\text{h}}33^{\text{m}}35^{\text{s}}243$  to  $01^{\text{h}}33^{\text{m}}35^{\text{s}}341$ . The vertical lines indicate the integration velocity ranges for figure 4. The three horizontal solid lines indicate the declination positions of MMSs 1–3. The beam size is shown in the top right corner. (Color online)

$\sim 132 \text{ km s}^{-1}$ , corresponding to the systemic velocity of the M 33GMC 37 region which was derived by a rotation model of the  $\text{HI}$  disk (Gratier et al. 2010). We note that

the  $^{12}\text{CO}(J = 2-1)$  line emission shows a wing-like profile with a velocity extent of more than  $5 \text{ km s}^{-1}$ . For position B, we find double-peak profiles in both the  $^{12}\text{CO}(J = 2-1)$  and  $^{13}\text{CO}(J = 2-1)$  line emissions, suggesting that there are two individual clouds toward the line of sight. We hereafter refer to the component at  $V_{\text{LSR}} = -143.0$  to  $-134.0 \text{ km s}^{-1}$  as the “blue cloud” and that at  $V_{\text{LSR}} = -133.0$  to  $-127.0 \text{ km s}^{-1}$  as the “red cloud.” On the other hand, the CO spectra of position C—the brightest peak in  $\text{C}^{18}\text{O}(J = 2-1)$ —show a single-peak profile for each line emission. Note that their central velocities of  $V_{\text{LSR}} \sim -133.5 \text{ km s}^{-1}$  roughly correspond to the mean velocity of the red and blue clouds.

Figures 4a and 4b show the spatial distributions of the blue and red clouds. The blue cloud is elongated in the northwestern direction, while the red cloud is stretched in the southwestern direction. Both clouds have filamentary CO structures. The typical width and length of filaments are  $\sim 3 \text{ pc}$  and  $\sim 10 \text{ pc}$ , respectively. The total mass is estimated to be  $\sim 2.4 \times 10^5 M_{\odot}$  for the blue cloud and  $\sim 1.9 \times 10^5 M_{\odot}$  for the red cloud using equations (1) and (2). Note that MMS 2 is likely associated not only with the brightest peak of the blue cloud, but also with that of the red cloud. The other continuum sources—MMSs 1 and 3—appear to be overlapped with both the red and blue clouds. The peak column density of molecular hydrogen is  $\sim 4.5 \times 10^{22} \text{ cm}^{-2}$  for the blue cloud, and  $\sim 4.1 \times 10^{22} \text{ cm}^{-2}$  for the red cloud.

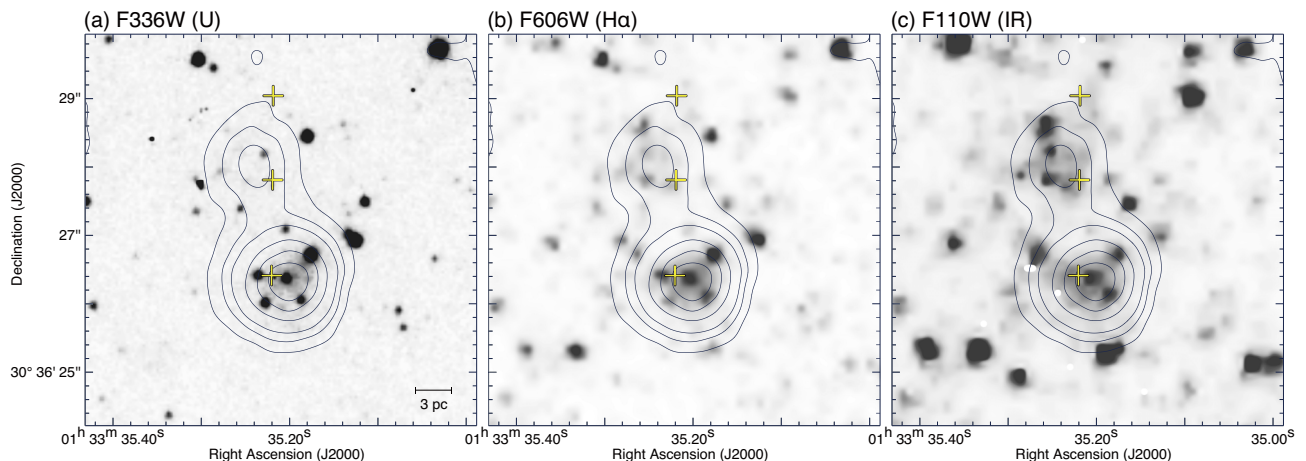


**Fig. 6.** Maps of optical images obtained with the Hubble Space Telescope (HST): (a) HST/WFC3 map with F336W filter ( $U$  band), (b) HST/WFPC2 map with F606W filter ( $H\alpha$ ), and (c) HST/WFC3 map with F110W filter (IR). The superposed contours and crosses are the same as in figure 4. The scale bar is also shown in the bottom right corner in panel (a).

We also find a small hole-like structure in the blue cloud centered at  $(\alpha_{\text{J}2000.0}, \delta_{\text{J}2000.0}) \sim (01^{\text{h}}35^{\text{m}}35^{\text{s}}28, 30^{\circ}36'27.''1)$ . Note that the peak positions of  $H\alpha$  and the millimeter continuum are placed on the edge of the hole-like structure, not on the center of it.

Figure 5 shows the position–velocity diagram of  $^{12}\text{CO}$  ( $J = 2-1$ ). The integration range in right ascension is from  $01^{\text{h}}33^{\text{m}}35.^s243$  to  $01^{\text{h}}33^{\text{m}}35.^s341$ , corresponding to the spatial extent of the small hole-like structure appearing in the blue cloud (see also figure 4a). The blue cloud is clearly seen; its radial velocity is centered at  $V_{\text{LSR}} \sim -137 \text{ km s}^{-1}$ . We find a V-shaped structure in the position–velocity diagram (see the dashed black lines in figure 5). The center velocity of the red cloud ( $V_{\text{LSR}} \sim -132 \text{ km s}^{-1}$ ) corresponds to the vertex of the V-shaped structure. The cavity-like structure and intensity peak of  $^{12}\text{CO}(J = 2-1)$  are seen at  $(\delta_{\text{J}2000.0}, V_{\text{LSR}}) \sim (30^{\circ}36'27.''1, -135.0 \text{ km s}^{-1})$  and  $(30^{\circ}36'26.''0, -134.0 \text{ km s}^{-1})$ , respectively.

## 4 Discussion

### 4.1 Presence of high-mass stars and their spectral types

Although there is no previous study of the stars embedded within the H<sub>II</sub> region in M 33, the detection of bright  $H\alpha$  emission, the 1.3 mm continuum sources MMSs 1–3, and 24  $\mu\text{m}$  emission indicates that several high-mass stars are associated with the two molecular clouds. To confirm the presence of high-mass stars, we compared them with archival optical datasets obtained with the Hubble Space Telescope (HST). Figure 6 shows the high spatial resolution optical images obtained with the HST WFPC2 and WFC3

detectors. The coordinate offsets of all datasets obtained with HST were corrected by comparing the position of the bright point sources with those catalogued in Gaia Data Release 2 (Gaia Collaboration 2018). We can clearly see  $\sim 10$  high-mass stars bright in the  $U$  band,  $H\alpha$ , and IR band within the Kitt Peak National Observatory (KPNO)  $H\alpha$  contours. Hereafter, we assume that ten high-mass stars are associated with the  $H\alpha$ , 1.3 mm continuum sources, and 24  $\mu\text{m}$  emission.

According to Verley et al. (2007), the luminosity of the 24  $\mu\text{m}$  emission is  $\sim 1.7 \times 10^{38} \text{ erg s}^{-1}$  and that of the  $H\alpha$  emission is  $\sim 4.6 \times 10^{37} \text{ erg s}^{-1}$  using the Spitzer MIPS and KPNO  $H\alpha$  datasets. To estimate the spectral types of high-mass stars we used two different methods. One estimates the total infrared luminosity  $L(\text{TIR})$  using the measured 24  $\mu\text{m}$  luminosity  $L(24 \mu\text{m})$  and the following equation (Verley et al. 2007):

$$\log L(\text{TIR}) = \log L(24 \mu\text{m}) + 0.908. \quad (3)$$

The total infrared luminosity of the high-mass stars is estimated to be  $\sim 1.4 \times 10^{39} \text{ erg s}^{-1}$ , which corresponds to ten O7.5V stars (Martins et al. 2005), assuming that the ten high-mass stars have the same spectral type.

The other method utilized the Lyman continuum luminosities  $N_{\text{Lyman}}$  (in units of photons) that are derived from extinction-corrected  $H\alpha$  luminosities  $L_{H\alpha}$  (in units of  $\text{erg s}^{-1}$ ) using the following equation (Mayya & Prabhu 1996):

$$N_{\text{Lyman}} = 7.3 \times 10^{11} L_{H\alpha}. \quad (4)$$

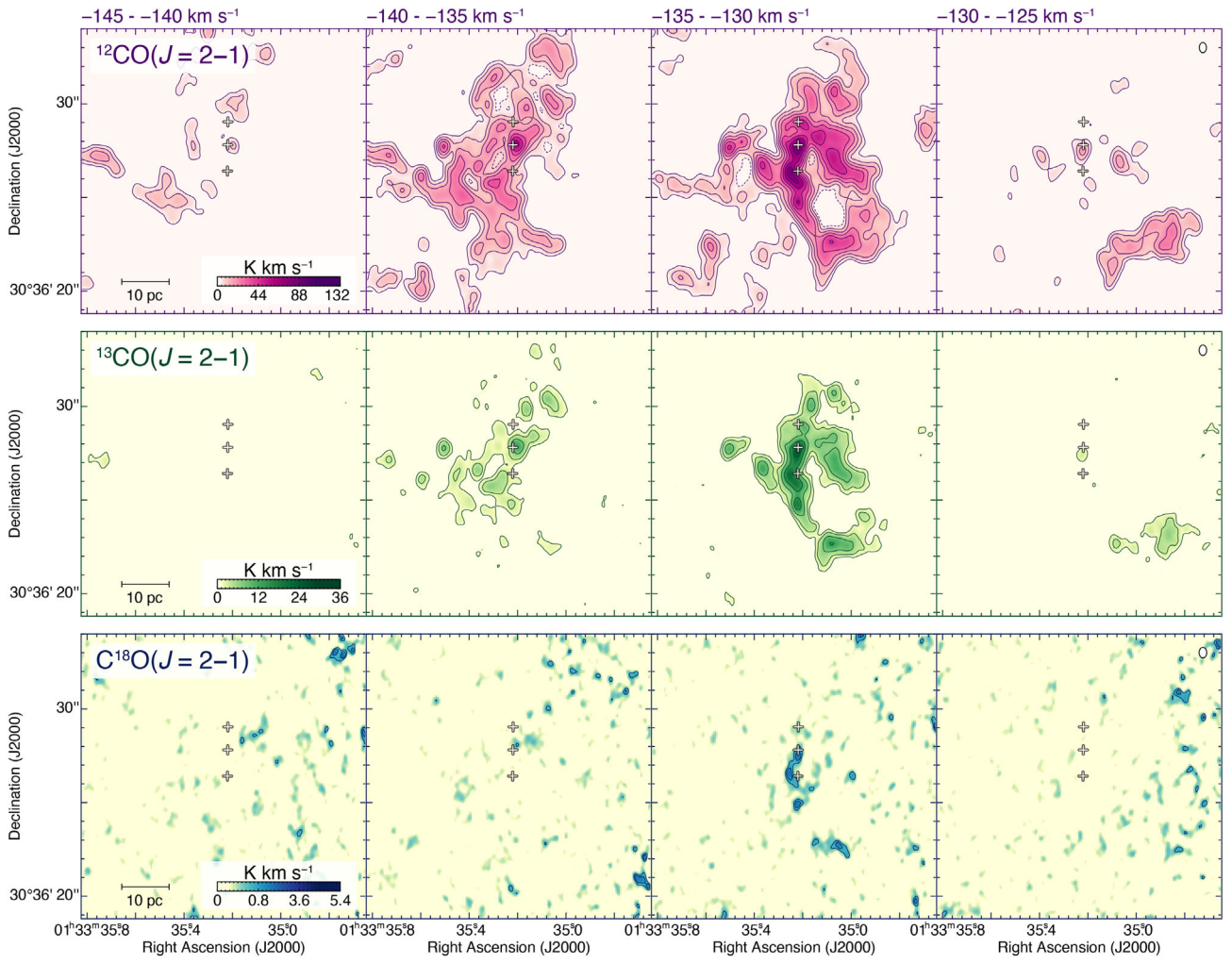


**Fig. 7.** Velocity channel maps of (a)  $^{12}\text{CO}(J = 2-1)$ , (b)  $^{13}\text{CO}(J = 2-1)$ , and (c)  $\text{C}^{18}\text{O}(J = 2-1)$  line emission toward M 33GMC 37. Each panel shows the intensity distribution integrated every  $5 \text{ km s}^{-1}$  in a velocity range from  $-145$  to  $-125 \text{ km s}^{-1}$ . The contour levels are  $4, 8, 14, 22, 32, 44, 58$ , and  $74 \text{ K km s}^{-1}$  for  $^{12}\text{CO}(J = 2-1)$ ;  $2, 4, 8$ , and  $14 \text{ K km s}^{-1}$  for  $^{13}\text{CO}(J = 2-1)$ ; and  $1.5, 2, 3$ , and  $5 \text{ K km s}^{-1}$  for  $\text{C}^{18}\text{O}(J = 2-1)$ . The beam size and scale bar are also shown in the top right and bottom left corner, respectively. The crosses indicate the positions of the millimeter continuum sources. (Color online)

We then obtain  $N_{\text{Lyman}} = 1.1 \times 10^{49}$  photons, corresponding to ten B0V stars (Martins et al. 2005). To summarize, the spectral types of high-mass stars embedded within M 33GMC 37 are estimated to be B0V–O7.5V assuming that there are ten high-mass stars of the same spectral type. Further detailed photometric and spectroscopic observations are needed to clarify the number of high-mass stars and their spectral types.

#### 4.2 Can stellar feedback explain the large velocity separation of the two clouds?

In the present study, we spatially resolved filamentary CO structures of M 33GMC 37 using ALMA with a spatial resolution of  $\sim 2 \text{ pc}$  ( $\Delta\theta \sim 0.^{\circ}5$ ). There are two individual

molecular clouds, red and blue, with a velocity separation of  $\sim 6 \text{ km s}^{-1}$  and a mass of  $\sim 2 \times 10^5 M_{\odot}$  for each. The densest part of the GMC is significantly detected in  $\text{C}^{18}\text{O}$  ( $J = 2-1$ ), containing up to  $\sim 10$  high-mass stars with spectral types B0V–O7.5V. In this section, we shall discuss whether the velocity separation of the two clouds can be explained by acceleration due to stellar feedback.

First, we claim that the total momentum of the stellar winds is significantly lower than that of the two molecular clouds. The typical wind momentum of an O-type star is calculated to be  $\sim 2 \times 10^3 M_{\odot} \text{ km s}^{-1}$ , by considering a mass accretion rate of  $\sim 10^{-6} M_{\odot} \text{ yr}^{-1}$ , a wind duration time of  $\sim 10^6 \text{ yr}$ , and a wind velocity of  $\sim 2000 \text{ km s}^{-1}$  (see Kudritzki & Puls 2000 and references therein). In the case of M 33GMC 37, the total wind momentum is therefore

$\sim 2 \times 10^4 M_{\odot} \text{ km s}^{-1}$ , assuming that there are ten O-type stars (see subsection 4.1). On the other hand, we derive a total cloud momentum of  $\sim 1.3 \times 10^6 M_{\odot} \text{ km s}^{-1}$ . Here we assume that the two clouds show an expanding motion with an expansion velocity of  $\sim 3 \text{ km s}^{-1}$ , corresponding to half the value of the velocity separation of the two clouds. Since the total cloud momentum is roughly two orders of magnitude higher than the total wind momentum, we conclude that the velocity separation of the two clouds cannot be explained by expanding gas motion due to stellar feedback.

This interpretation is also consistent with the velocity distributions of the two clouds. If the expansion of the clouds is centered at an exciting star, a ring-like gas distribution would be expected not only in the spatial distribution such as the moment 0 map, but also in the position–velocity diagram (cf. figure 8 in Torii et al. 2015). For M33GMC 37, however, we could not find such distributions around the 3 mm continuum sources (see figures 3 a and 5). We have also created velocity channel maps in order to justify the velocity and spatial distributions of the clouds, because expanding clouds will be spatially shifted from inward to outward in the velocity channel maps (e.g., Fukui et al. 2012; Sano et al. 2017b). Figure 7 shows the velocity channel maps for each CO line emission. We confirmed that there are no clear signs of such spatial shifts with increasing velocity. On the other hand, we note that a tiny CO clump near MMS 2 appears in all velocity ranges of the  $^{12}\text{CO}(J = 2-1)$  line emission, suggesting possible evidence of outflowing gas in addition to the wing-like profile of MMS 1 (figure 2a). Although the outflowing gas candidate is very concentrated, within 1 pc scales, the outflowing gas could not strongly affect the dynamical motion of the two clouds. To summarize, the stellar feedback effect is negligible for the cloud kinematics, and therefore the velocity separation of the two clouds cannot be explained by acceleration by stellar winds and outflowing gas.

### 4.3 An alternative idea: High-mass star formation triggered by cloud–cloud collisions in M33GMC 37

In the previous section we concluded that the velocity separation of the two clouds is not caused by the stellar feedback effect. It is therefore reasonable to assume that the two individual clouds have collided with each other and have formed the high-mass stars embedded within M33GMC 37. In this section we discuss this second scenario.

To form high-mass stars via cloud–cloud collisions, a supersonic velocity separation of the two colliding clouds is essential. According to magnetohydrodynamical numerical simulations, the effective Jeans mass in the

shock-compressed layer is proportional to the third power of the effective sound speed (Inoue & Fukui 2013). Here, the effective sound speed is defined as  $(c_s^2 + c_A^2 + \Delta v^2)^{0.5}$ , where  $c_s$  is the sound speed,  $c_A$  is the Alfvén speed, and  $\Delta v$  is the velocity dispersion. A supersonic velocity separation of at least a few  $\text{km s}^{-1}$  therefore produces a large mass accretion rate, on the order of  $\sim 10^{-4}\text{--}10^{-3} M_{\odot} \text{ yr}^{-1}$ , which allows mass growth of stars against the stellar feedback (Inoue & Fukui 2013). For the case of M33GMC 37, the observed velocity separation of the red and blue clouds is  $\sim 6 \text{ km s}^{-1}$  (see the CO spectra in figure 2b). Although the velocity separation will be changed due to the projection effect, this is roughly consistent with the typical velocity separation in the Galactic high-mass star-forming regions triggered by cloud–cloud collisions: e.g., M20 ( $\sim 7.5 \text{ km s}^{-1}$ , Torii et al. 2011), RCW 36 ( $\sim 5 \text{ km s}^{-1}$ , Sano et al. 2018), M42 ( $\sim 7 \text{ km s}^{-1}$ , Fukui et al. 2018a), and RCW 166 ( $\sim 5 \text{ km s}^{-1}$ , Ohama et al. 2018).

We next focus on the velocity structures of the two colliding clouds. Previous numerical simulations and observational results have demonstrated that colliding clouds create an intermediate velocity component—bridging feature—connecting two clouds due to the deceleration by collisions, if the projected velocity separation is significantly larger than the linewidth of the colliding clouds (see Fukui et al. 2018a and references therein). When the two colliding clouds have roughly the same column density of gas, the two clouds will be merged and appear as a single-peak CO profile centered at the mean velocity of the two colliding clouds (e.g., Fukui et al. 2017). In the case of M33GMC 37, the  $V_{\text{LSR}} \sim -135 \text{ km s}^{-1}$  feature in the  $^{13}\text{CO}$  spectrum at position A is possibly a bridging feature (see figure 2b), but is not significantly detected because of the small velocity separation of the two colliding clouds. However, the CO spectra at position B—the densest part of the colliding clouds—show single-peak CO profiles centered at  $V_{\text{LSR}} \sim -133.5 \text{ km s}^{-1}$ , roughly corresponding to the mean velocity of the red and blue clouds (see also figure 2c). This is consistent with the two clouds having roughly the same column density of  $\sim 4\text{--}5 \times 10^{22} \text{ cm}^{-2}$ , assuming cloud–cloud collision has occurred.

The V-shaped structure in the position–velocity diagram as shown in figure 5 provides us with suggestive evidence for head-on cloud–cloud collision. As discussed above, an intensity depression or a hole-like structure might indicate the spot of collision between two clouds for the case of a head-on collision. If we make a position–velocity diagram that includes the collision region, we can find not only the bridging feature but also the V-shaped structure (e.g., Fukui et al. 2018a, 2018c, 2018d; Hayashi et al. 2018; Torii et al. 2018a, 2018b; Fujita et al. 2019b). Note that if an oblique collision—e.g., collisions with the edges of the

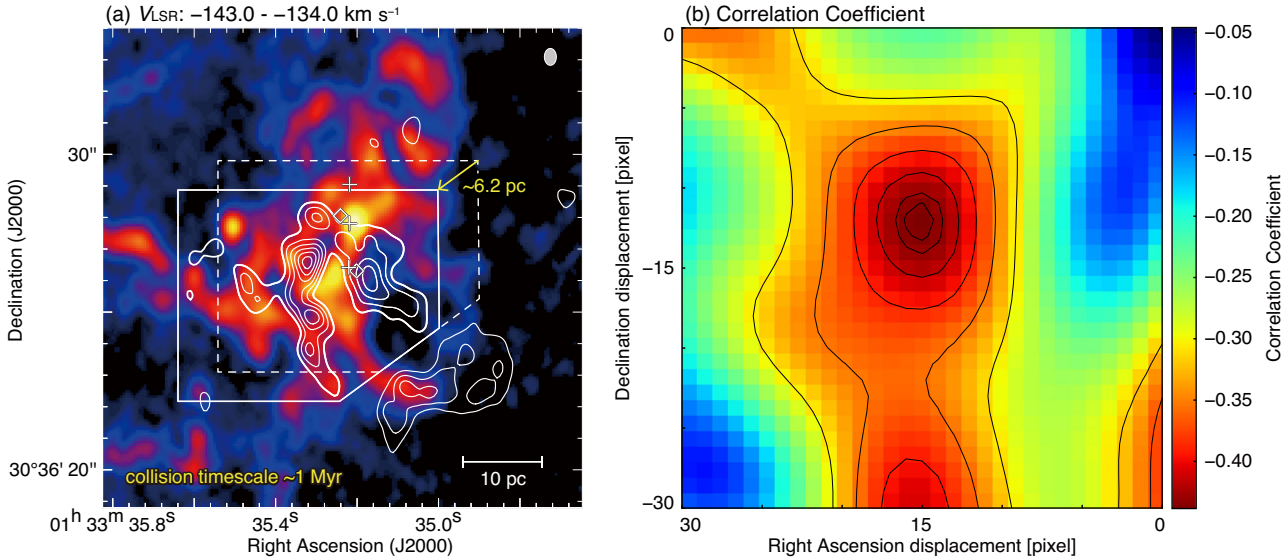


**Fig. 8.** (a) Complementary spatial distribution of the red (contours) and blue clouds (image). The velocity ranges of image and contours are the same as shown in figures 4a and 4b, respectively. The contour levels are 16, 26, 36, 46, 56, and 66 K  $\text{km s}^{-1}$ . The contours are spatially displaced  $\sim 6.2$  pc in the southeast direction (P.A. = 137°). The dashed and solid rectangles indicate the before and after displacement of the contours, respectively. The crosses and diamonds are the same as shown in figure 2. The scale bar and beam size are also shown in the bottom and top right corner, respectively. (b) Map of Pearson's correlation coefficient as a function of displacements in the right ascension direction and in the declination direction in pixel units. The size of a pixel is 84.5 mas. The coordinate origin is  $(\alpha_{\text{J2000.0}}, \delta_{\text{J2000.0}}) = (01^{\text{h}}33^{\text{m}}35^{\text{s}}22, 30^{\circ}36'27''5)$ . The intensity distributions of  $^{12}\text{CO}(J=2-1)$  enclosed by the dashed polygon (blue cloud) and the solid polygon (red cloud) were used to calculate the correlation coefficient. The superposed contours indicate the values of the correlation coefficients, whose levels are  $-0.435, -0.430, -0.415, -0.390, -0.355$ , and  $-0.310$ . (Color online)

clouds—occurred, we could not find such a V-shaped structure in the position–velocity diagram (Fujita et al. 2020a). For M 33GMC 37, we can clearly see the V-shaped structure connecting the red and blue clouds as the intermediate velocity component that is called the bridging feature. Moreover, the presence of an intensity peak and depression in the V-shaped structure is predicted by synthetic observations of a theoretical result of a head-on cloud–cloud collision (e.g., Fukui et al. 2018c).

Another important signature of a collision is complementary spatial distribution of the colliding clouds. In general, colliding clouds are not the same size, such as simulated by Habe and Ohta (1992) and Anathpindika (2010). In fact, observational results indicate that colliding clouds have different sizes, morphologies, and density distributions (e.g., Hasegawa et al. 1994; Furukawa et al. 2009; Fukui et al. 2014, 2018a, 2018b; Enokiya et al. 2018; Tokuda et al. 2018; Dewangan et al. 2019a, 2019b). In such cases, one of the colliding clouds can create a hole-like structure in the other cloud, if the colliding cloud has a denser part and/or smaller size than the other cloud. This produces a complementary spatial distribution of two clouds with different systematic velocity. Furthermore, the angle of the two colliding clouds  $\theta$  is generally not 0° or 90° relative to the line of sight. This means that we can also observe a spatial displacement between the complementary distributions of two clouds.

To evaluate such complementary distributions of two colliding clouds, it is useful to calculate the correlation coefficient between the intensity distributions of the two clouds (cf. Fujita et al. 2020b). If the correlation coefficient between the two colliding clouds shows a negative value, the two clouds show complementary spatial distributions. The lower the correlation coefficient, the higher the complementarity. By changing the values of the spatial displacement for one of the colliding clouds, we can obtain a map of the correlation coefficient between the two clouds as a function of displacement. The best-fitting value of the displacement for each coordinate can be derived as the point of local minimum.

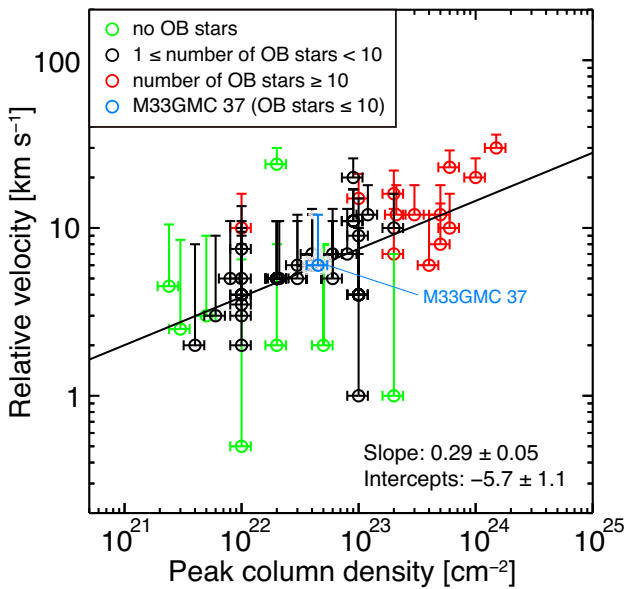
In M 33GMC 37, we find complementary spatial distributions of the red and blue clouds by following the above method. Figure 8a shows the map of the blue cloud superposed on the red cloud contours with a spatial displacement of  $\sim 6.2$  pc toward the southeast direction. The brightest peak of the red cloud fits within the hole-like structure of the blue cloud. The second and third minor peaks of the red cloud also show good complementary distributions (or anti-correlation) with the blue cloud. Figure 8b shows the map of the correlation coefficient between the two clouds as a function of the spatial displacement of the red cloud in the directions of right ascension and declination. Since the cloud collision in M 33GMC 37 is likely a head-on collision, the correlation coefficients were calculated toward the inner

parts of the blue cloud. We can find the local minimum with a correlation coefficient of  $-0.44$  at a shift by 15 pix in RA and  $-12$  pix in Dec, which is significantly lower than the correlation coefficient of  $-0.05$  without displacement. We also calculate a  $p$ -value which provides information about whether a statistical hypothesis is significant or not. As a result, the correlation coefficient of  $-0.44$  is significant at the 0.5% significance level.

If the cloud collision scenario is correct, we can also estimate the collision time scale as a dynamical time scale using the values of the displacement and velocity difference of the two clouds of (spatial displacement)/(velocity difference) =  $8.8 \text{ pc}/8.5 \text{ km s}^{-1} \sim 1 \text{ Myr}$ , assuming a collision angle of  $\theta = 45^\circ$ . Since GMCs are thought to be dispersed within  $\sim 1.5 \text{ Myr}$  due to strong stellar winds and UV radiation (Kruijssen et al. 2019), the shorter collision time scale is consistent with the presence of dense molecular clouds surrounding the high-mass stars and small H II regions with a few pc extent in H $\alpha$  emission because of the young age of the high-mass stars (see figures 1b and 4).

We also note that the number of high-mass stars ( $\lesssim 10$ ) in M 33GMC 37 is consistent with previous observational studies of cloud–cloud collisions. According to Fukui et al. (2018a), the formation of super star clusters containing more than ten O-type stars requires collisions of two dense clouds, one of which has a high column density of at least  $\sim 10^{23} \text{ cm}^{-2}$  (e.g., RCW 38, Fukui et al. 2016; NGC 3603, Fukui et al. 2014; Westerlund 2, Furukawa et al. 2009). On the other hand, the formation of single or a few O-type stars happens in a collision between molecular clouds with low column density of several  $10^{22} \text{ cm}^{-2}$  or less (e.g., RCW 120, Torii et al. 2015; NGC 2359, Sano et al. 2017a; S44, Kohno et al. 2018b; N4, Fujita et al. 2019a; more detailed results are summarized in Enokiya et al. 2019). For M 33GMC 37, the two colliding clouds have a low column density of  $\sim 4\text{--}5 \times 10^{22} \text{ cm}^{-2}$ . Therefore, cloud–cloud collisions in M 33GMC 37 can create  $\sim 10$  high-mass stars at most. This is consistent with  $\sim 10$  stars being detected by HST optical images within the KPNO H $\alpha$  boundary (see figure 6).

In addition, Enokiya, Torii, and Fukui (2019) recently revealed that the number of OB stars formed in cloud collisions depends not only on the column density, but also on the velocity difference of the two colliding clouds. Figure 9 shows a correlation plot between the column density and relative velocity toward the sites of cloud–cloud collisions in the Milky Way (Enokiya et al. 2019). The authors found that too fast or slow cloud collisions cannot form OB stars even if the cloud column density is high enough. In the case of M 33GMC 37, the observational parameters are consistent with the trend seen in previous studies. This possibly indicates that there is no critical difference between



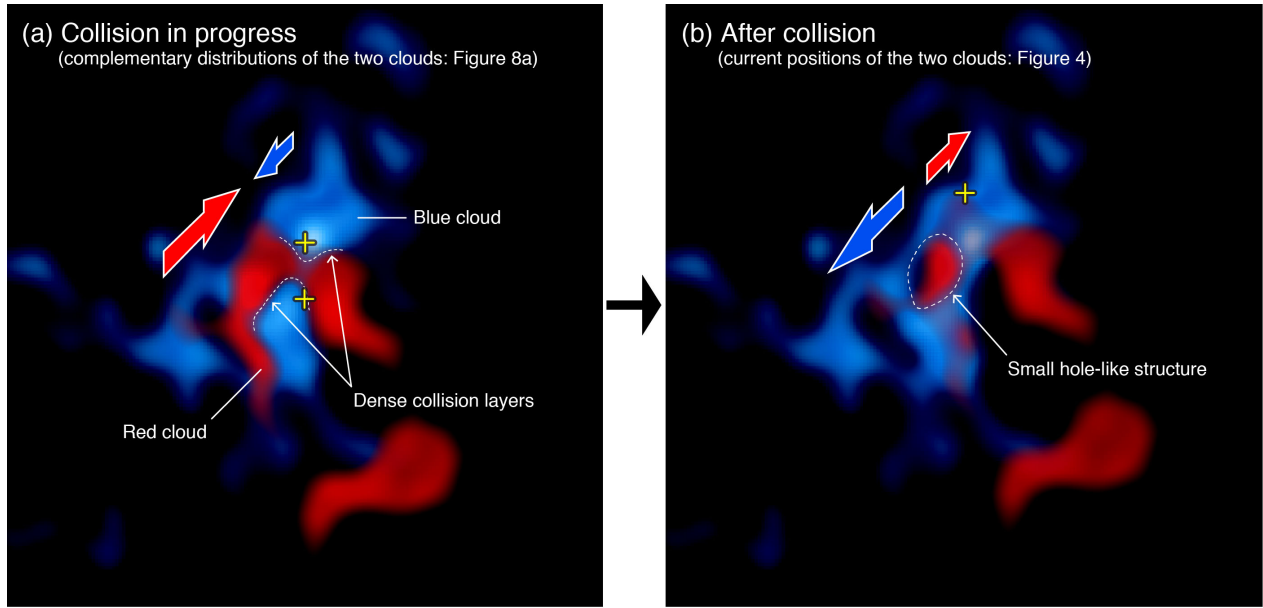


**Fig. 10.** Schematic images of the cloud–cloud collisions in M 33GMC 37 for the phases of (a) collision in progress and (b) after collision. The red and blue colors represent the red and blue clouds, respectively. The red and blue arrows indicate the directions of movement of the red and blue clouds, respectively. The dense collision layers and the small hole-like structure in the blue cloud are also indicated. The yellow crosses indicate the positions of MMSs 1–3. (Color online)

diagram are also consistent with the positions of the dense collision layers and the hole-like structure in the blue cloud, respectively (figure 5).

To summarize, the red and blue clouds in M 33GMC 37 fulfill four requirements of high-mass star formation triggered by cloud–cloud collisions, as follows: (1) supersonic velocity separation of the two clouds, (2) complementary spatial distribution with the displacement of the colliding clouds, (3) the presence of a bridging feature connecting the two clouds in velocity space, and (4) a V-shaped structure in the position–velocity diagram. We therefore suggest that the high-mass stars corresponding to ten B0V–O7.5V types in M 33GMC 37 were formed by cloud–cloud collisions. Further ALMA observations of M 33 GMCs will allow us to study high-mass star formation via cloud–cloud collisions in the spiral galaxy, the results of which can be directly compared with the Milky Way and Magellanic Clouds.

## 5 Conclusion

In the present study, we carried out new CO( $J = 2-1$ ) and continuum observations of M 33GMC 37 using ALMA with an angular resolution of  $\sim 0''.5$ , corresponding to a spatial resolution of  $\sim 2$  pc at the distance of M 33. We revealed two individual molecular clouds with a velocity separation of  $\sim 6 \text{ km s}^{-1}$  that are associated with up to  $\sim 10$  high-mass stars of spectral types B0V–O7.5V. The two

molecular clouds show complementary spatial distribution with a spatial displacement of  $\sim 6.2$  pc. An intermediate velocity component of the two clouds as a V-shaped structure in the position–velocity diagram was also detected. We proposed a possible scenario whereby the high-mass stars in M 33GMC 37 were formed by cloud–cloud collisions approximately 1 Myr ago.

## Acknowledgment

This paper makes use of the following ALMA data: ADS/JAO ALMA#2018.1.00378.S. ALMA is a partnership of ESO (representing its member states), NSF (USA), and NINS (Japan), together with NRC (Canada), NSC and ASIAA (Taiwan), and KASI (Republic of Korea), in cooperation with the Republic of Chile. The Joint ALMA Observatory is operated by ESO, AUI/NRAO, and NAOJ. Based on observations made with the NASA/ESA Hubble Space Telescope, and obtained from the Hubble Legacy Archive, which is a collaboration between the Space Telescope Science Institute (STScI/NASA), the Space Telescope European Coordinating Facility (ST-ECF/ESA), and the Canadian Astronomy Data Centre (CADC/NRC/CSA). This study was financially supported by Grants-in-Aid for Scientific Research (KAKENHI) of the Japanese Society for the Promotion of Science (JSPS, grant nos. 16K17664, 18J01417, and 19K14758). K. Tokuda was supported by NAOJ ALMA Scientific Research Grant Number 2016-03B. H.S. was also supported by the ALMA Japan Research Grant of NAOJ Chile Observatory (grant no. NAOJ-ALMA-226). M.S. acknowledges support by the Deutsche Forschungsgemeinschaft through the Heisenberg professor grants SA 2131/5-1 and 12-1. We are also grateful to the anonymous referee for useful comments which helped the authors to improve the paper.

## References

- Anathpindika, S. V. 2010, MNRAS, 405, 1431
- Cornwell, T. J. 2008, IEEE J-STSP, 2, 793
- Dewangan, L. K., Ojha, D. K., Baug, T., & Devaraj, R. 2019a, ApJ, 875, 138
- Dewangan, L. K., Sano, H., Enokiya, R., Tachihara, K., Fukui, Y., & Ojha, D. K. 2019b, ApJ, 878, 26
- Druard, C., et al. 2014, A&A, 567, A118
- Enokiya, R., et al. 2018, PASJ, 70, S49
- Enokiya, R., Torii, K., & Fukui, Y. 2019, PASJ, in press (doi: 10.1093/pasj/psz119)
- Freedman, W. L., et al. 2001, ApJ, 553, 47
- Fujita, S., et al. 2019a, ApJ, 872, 49
- Fujita, S., et al. 2019b, PASJ, in press (doi: 10.1093/pasj/psz025)
- Fujita, S., et al. 2020a, PASJ, in press (doi: 10.1093/pasj/psaa005)
- Fujita, S., et al. 2020b, PASJ, submitted (arXiv:2003.13925)
- Fukui, Y., et al. 2012, ApJ, 746, 82
- Fukui, Y., et al. 2014, ApJ, 780, 36
- Fukui, Y., et al. 2015, ApJ, 807, L4
- Fukui, Y., et al. 2016, ApJ, 820, 26
- Fukui, Y., et al. 2018a, ApJ, 859, 166
- Fukui, Y., et al. 2018b, PASJ, 70, S41
- Fukui, Y., et al. 2018c, PASJ, 70, S44
- Fukui, Y., et al. 2018d, PASJ, 70, S46
- Fukui, Y., et al. 2019, ApJ, 886, 14
- Fukui, Y., Tsuge, K., Sano, H., Bekki, K., Yozin, C., Tachihara, K., & Inoue, T. 2017, PASJ, 69, L5
- Furukawa, N., Dawson, J. R., Ohama, A., Kawamura, A., Mizuno, N., Onishi, T., & Fukui, Y. 2009, ApJ, 696, L115
- Gaia Collaboration, 2018, A&A, 616, A1
- Gratier, P., et al. 2010, A&A, 522, A3
- Gratier, P., et al. 2012, A&A, 542, A108
- Habe, A., & Ohta, K. 1992, PASJ, 44, 203
- Hasegawa, T., Sato, F., Whiteoak, J. B., & Miyawaki, R. 1994, ApJ, 429, L77
- Hayashi, K., et al. 2018, PASJ, 70, S48
- Inoue, T., & Fukui, Y. 2013, ApJ, 774, L31
- Inoue, T., Hennebelle, P., Fukui, Y., Matsumoto, T., Iwasaki, K., & Inutsuka, S. 2018, PASJ, 70, S53
- Kohno, M., et al. 2018a, PASJ, 70, S50
- Kohno, M., et al. 2018b, PASJ, in press (doi: 10.1093/pasj/psy109)
- Kruijssen, J. M. D., et al. 2019, Nature, 569, 519
- Kudritzki, R.-P., & Puls, J. 2000, ARA&A, 38, 613
- McMullin, J. P., Waters, B., Schiebel, D., Young, W., & Golap, K. 2007, in ASP Conf. Ser., 376, Astronomical Data Analysis Software and Systems XVI, ed. R. A. Shaw et al. (San Francisco: ASP), 127
- Martins, F., Schaerer, D., & Hillier, D. J. 2005, A&A, 436, 1049
- Massey, P., Olsen, K. A. G., Hodge, P. W., Strong, S. B., Jacoby, G. H., Schlingman, W., & Smith, R. C. 2006, AJ, 131, 2478
- Mayya, Y. D., & Prabhu, T. P. 1996, AJ, 111, 1252
- Miura, R. E., et al. 2012, ApJ, 761, 37
- Ohama, A., et al. 2018, PASJ, 70, S47
- Saigo, K., et al. 2017, ApJ, 835, 108
- Sano, H., et al. 2017a, arXiv:1708.08149
- Sano, H., et al. 2017b, J. High Energy Astrophys., 15, 1
- Sano, H., et al. 2018, PASJ, 70, S43
- Shima, K., Tasker, E. J., Federrath, C., & Habe, A. 2018, PASJ, 70, S54
- Tachihara, K., Gratier, P., Sano, H., Tsuge, K., Miura, R. E., Muraoka, K., & Fukui, Y. 2018, PASJ, 70, S52
- Takahira, K., Tasker, E. J., & Habe, A. 2014, ApJ, 792, 63
- Tokuda, K., et al. 2018, ApJ, 862, 8
- Tokuda, K., et al. 2019, ApJ, 886, 15
- Torii, K., et al. 2011, ApJ, 738, 46
- Torii, K., et al. 2015, ApJ, 806, 7
- Torii, K., et al. 2018a, PASJ, 70, S51
- Torii, K., et al. 2018b, PASJ, in press (doi: 10.1093/pasj/psy098)
- Tosaki, T., et al. 2011, PASJ, 63, 1171
- Tsuge, K., et al. 2019, ApJ, 871, 44
- Verley, S., Hunt, L. K., Corbelli, E., & Giovanardi, C. 2007, A&A, 476, 1161
- Zinnecker, H., & Yorke, H. W. 2007, ARA&A, 45, 481